



CARBON BASED SMART SYSTEM FOR WIRELESS APPLICATION



Start Date : 30/11/13
Project n°318352

Duration : 48 months

Topic addressed: Very advanced nanoelectronic components: design, engineering, technology and manufacturability

WORK PACKAGE 4: Test activities

DELIVERABLE D4.7

Activity Report on parameter extraction procedure for DC and HF models for CNT based sub-modules

Due date: T0+40

Submission date : T0+48

Lead contractor for this deliverable: Tyndall

Dissemination level: PU – Public

WORK PACKAGE 4: Test activities

PARTNERS ORGANISATION APPROVAL

	Name	Function	Date	Signature
Prepared by:	M.Modreanu	R&D Engineer	04/10/2016	
Prepared by:	M.Dragoman	R&D Engineer	04/10/2016	
Prepared by:	C.Tripon Canseliet	R&D Engineer	04/10/2016	
Prepared by:	G.Deligeorgis	R&D Engineer	04/10/2016	
Prepared by:	F.Coccheti	R&D Engineer	04/10/2016	
Approved by:	A.Ziaei	Research Program Manager	06/10/2016	

DISTRIBUTION LIST

QUANTITY	ORGANIZATION		NAMES
1 ex	Thales Research and Technology	TRT	Afshin ZIAEI
1 ex	Chalmers University of Technology	CHALMERS	Johan LIU
1 ex	Foundation for Research & Technology - Hellas	FORTH	George KONSTANDINIS
1 ex	Laboratoire d'Architecture et d'Analyse des Systèmes	CNRS-LAAS	Patrick PONS
1 ex	Université Pierre et Marie Curie	UPMC	Charlotte TRIPON-CANSELIET
1 ex	National Research and Development Institute for Microtechnologies	IMT	Mircea DRAGOMAN
1 ex	Graphene Industries	GI	Peter BLAKE
1 ex	Thales Systèmes Aéroportés	TSA	Yves MANCUSO
1 ex	SHT Smart High-Tech AB	SHT	Yifeng FU
1 ex	Universita politecnica delle Marche	UNIVPM	Luca PIERANTONI
1 ex	Linköping University	LiU	Rositsa YAKIMOVA
1 ex	Fundacio Privada Institute Catala de Nanorfnologia	ICN	Clivia SOTOMAYOR
1 ex	Tyndall-UCC	Tyndall	Mircea MODREANU



D4.7: Activity Report on parameter extraction procedure for DC and HF models for CNT based sub-modules

3/21

CHANGE RECORD SHEET

REVISION LETTER	DATE	PAGE NUMBER	DESCRIPTION
Template	25/01/2016		
V1	06/10/2016	21	Final version

CONTENTS

1 EXECUTIVE SUMMARY	5
2 PARAMETER EXTRACTION PROCEDURE FOR CNT-FET	5
3 PARAMETER EXTRACTION PROCEDURE FOR GRAPHENE-FET	5
4 MODELING AND OPTIMISATION OF THE GRAPHENE DETECTOR.....	6
4.1 DEVICE RF SIMULATION	7
4.2 DEVICE OPTIMIZATION	9
5 DESIGN AND FABRICATION OF THE GRAPHENE COPLANAR PATCH ANTENNA (CPA)...	10
6 EXPERIMENTAL CHARACTERIZATION OF THE GRAPHENE COPLANAR PATCH ANTENNA (CPA) AT MICROWAVE FREQUENCIES	11
7 THE X BAND SLOT ANTENNA LOADED WITH A GRAPHENE PATCH	16
7.1 ELECTROMAGNETIC MODEL AND SIMULATION RESULTS	16
7.2 MEASUREMENT RESULTS	18
8 CONCLUSION & PERSPECTIVES.....	21

1 EXECUTIVE SUMMARY

This deliverable covers WP4 activities on parameter extraction procedure for DC and HF model for CNT and graphene submodules fabricated in WP3.

2 PARAMETER EXTRACTION PROCEDURE FOR CNT-FET

2.1 Extraction of the transconductance g_m of a CNT-FET: numerical example.

In the ballistic limit, the equivalent circuit of a CNT-FET obtained by self-consistent modelling includes a transconductance **g_m in the order of 1-10 μS** , depending on metal work function and gate-oxide thickness/permittivity.

An example of current-voltage characteristic is reported in Fig. 1.

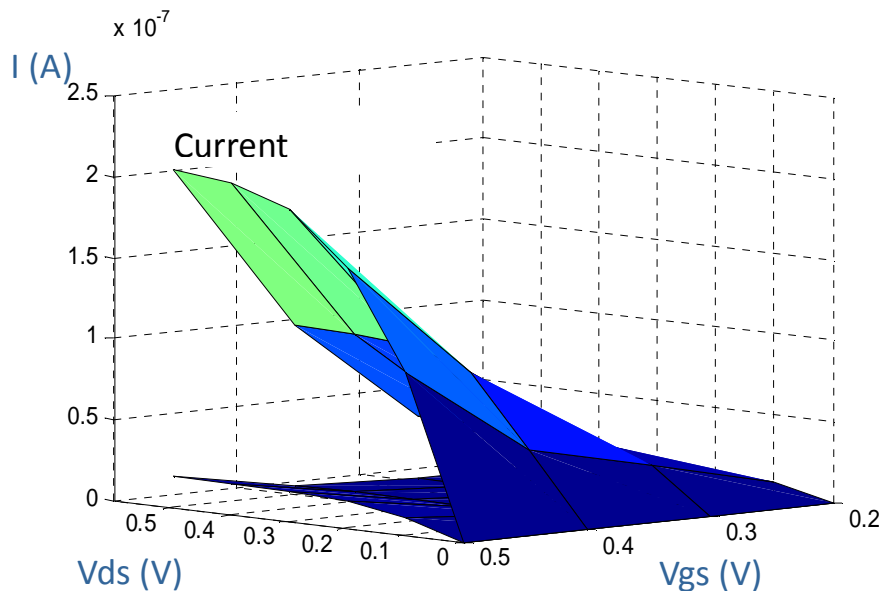


Fig. 1. I- V_{ds} characteristics for different applied gate and drain voltages for CNT-FET. The upper and lower surface are obtained with a metal work function of 4.4 eV and 4.5 eV respectively. Simulation detail: CNT Length = 50nm, cylindrical gate of radius = 15nm, relative dielectric permittivity = 5, working point: $V_{gs} = 0.4\text{V}$, $V_{ds} = 0.5\text{V}$.

As a further example, in case of a 200 nm long semiconducting CNT, a gate thickness of 15nm, and relative dielectric permittivity equal to 5:

the transconductance is numerically estimated by typical values of a few μS .

Of course, increasing the permittivity, and reducing gate thickness, provides good agreement with the achieved experimental transconductance of **110 mS/mm**, which is equivalent to a value of about **10 μS per CNT**, if we assume an actual CNT density of **11 μm^{-1}** .

3 PARAMETER EXTRACTION PROCEDURE FOR GRAPHENE-FET

3.1 Extraction of the transconductance g_m of a graphene FET: numerical examples.

In order to estimate the transconductance of a graphene FET (G-FET), we plot the current-voltage characteristics in the quasi static limit: these are shown in Fig. 2 for a G-FET with channel length of

600 nm, gate length 200 nm, dielectric thickness of 10 nm, $\epsilon_r=25$. The Fermi level μ of graphene is assumed equal to 0 eV.

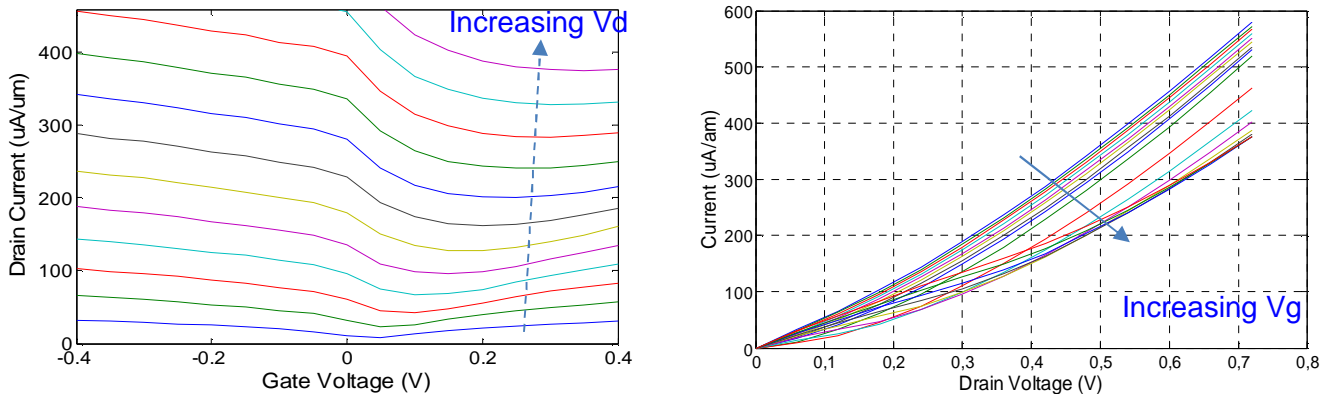


Fig. 2. a) current/gate-voltage characteristic for different drain-voltages (V_d in the range [0 V, 0.72 V]), b) Current/drain-voltage characteristic for different gate-voltages (V_g in the range [-0.4 V, 0.5 V]).

The above operative conditions closely resemble those of the experiments.

It is clear from Fig. 2 that, depending on the working point (drain and gate voltages), the transconductance g_m of the device is in the range between about **100 and 500 $\mu\text{S}/\mu\text{m}$** , which is larger than the experimental value, i.e. **40 $\mu\text{S}/\mu\text{m}$** . Correspondingly, the absolute values of the experimental currents are about 3 to 5 times lower than theoretical predicted ones.

The above comparison between theory and experiments is in reasonable accordance with what expected from the fact that, in the present ballistic approach, the channel ohmic-resistivity is not accounted (of course, it could be estimated and included in the model, in order to match the experiments). From these considerations, we can deduce that the ballistic length of the available graphene samples is probably lower than the channel length, i.e. 600 nm, although a correct estimation of the ballistic length should include also the effect graphene-metal contact resistance.

4 MODELING AND OPTIMISATION OF THE GRAPHENE DETECTOR

The simulation and optimization by high frequency simulation software and lumped element equivalent circuit of the graphene detector designed and fabricated within the NANORF project by LAAS and FORTH is here reported¹. The device is based on the non linearity I-V characteristic introduced by the concept of ballistic transport taking place therein^{2,3}.

Device description

The device is based on an original design⁴, has two RF ports (150 μm pitch) that are tapered down to a coplanar waveguide with a 2 μm signal – ground electrode gap. This enables the matching of size with the mean free path typically observed in graphene (400nm). The input port leads to a discontinuous signal electrode. In the CPW gap, a series of Y-branched graphene ribbons are formed from a continuous monolayer graphene using e-beam lithography and oxygen plasma etching so that

¹ F. Coccetti, R. Plana and G. Deligeorgis, "Modeling and optimization of a RF ballistic graphene demodulator," in proceedings of IEEE International Microwave Symposium Seattle 1-7 June 2013

² C. Sinha and R. Biswas, "Unconventional ballistic transport through bilayer graphene electrostatic barriers," *Phys. Rev. B*, vol. 84, no. 15, p. 155439, Oct. 2011

³ H. Irie, Q. Diduck, M. Margala, R. Sobolewski, and M. J. Feldman, « Nonlinear characteristics of T-branch junctions: Transition from ballistic to diffusive regime, » *Appl. Phys. Lett.* 93, 53502 (2008).

⁴ G. Deligeorgis, F. Coccetti, G. Konstantinidis and R. Plana, "Radio frequency signal detection by ballistic transport in Y-shaped graphene nanoribbons," *Applied Physics Letters* 101, 013502 (2012)

the two branches are in contact with the signal and the ground electrodes respectively. The third branch of each ribbon resides at the center of the coplanar waveguide port.

To contact the bottom edge of each nanoribbon, without contacting the center of the “Y” shaped graphene junction, a metallic air-bridge is formed between adjacent bottom electrodes. The latter is electrically connected to the signal electrode that leads to the output port (right port in Fig.3). Electron beam lithography was used to fabricate the device. No post-treatment was performed.

The RF response of the device was measured using a VNA setup. To identify the effect of the graphene Y-junctions and facilitate de-embedding, a similar device without graphene was also fabricated and measured. S_{11} and S_{12} are shown for both cases in Fig.4.

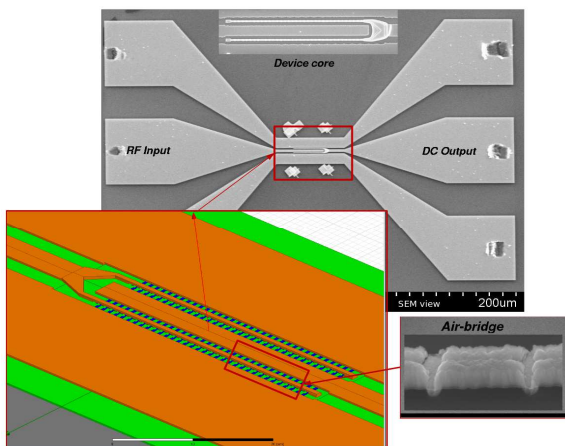


Figure 3: Optical microscope image of the device. Top inset shows a schematic of the Y-junction ribbon made from graphene. Bottom inset shows an electron microscope view of the air-bridge structure

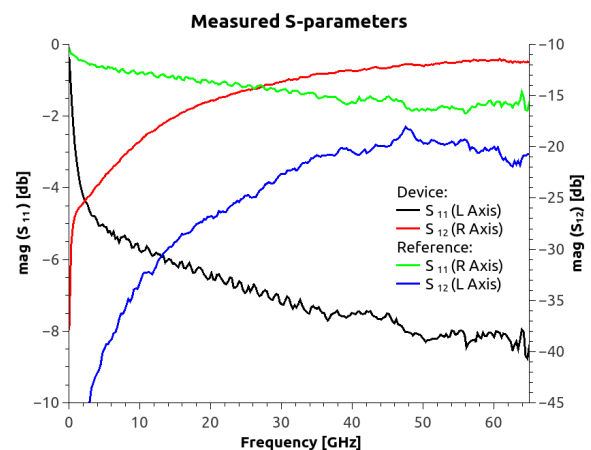


Figure 4: Example of measured S parameters for the fabricated device and the reference (no Graphene)

As expected, there is a significant reflection drop due to the conduction of graphene Y-junctions which act as a shunt resistance in the input port thus reducing the reflected power. Similarly, there is an increase in the transmission due to the fact that the output port is now resistively coupled with the input network. It should be noted that ideally the input reflection should be negligible if the graphene resistance was matched to the device impedance.

The central idea of this device lies on the ballistic transport of charges inside the Y-junction ribbon. As shown in Fig.5, the trajectory of a ballistic electron differs from that of an electron diffusing through several scattering events. In the former case charges end up in the bottom branch of the ribbon and get picked up by the output port thus creating a DC response shown in Fig.5. Such a device has potential to operate well above existing Schottky diode demodulators⁵. In the following of this report the analysis and the lumped elements equivalent circuit extraction is presented. This will explain the device performance and demonstrate how to optimise the design even further.

4.1 DEVICE RF SIMULATION

The device topology was simulated using HFSS RF simulation software. Initially the metallic electrodes were modelled without taking into account the graphene junctions. This was compared to the reference device described previously. Subsequently, the graphene Y-junctions were modelled assuming resistive 2-D layer behaviour in HFSS. This choice was justified by previous studies⁶. The sheet resistance of the material was used as a free parameter to fit the simulation results to the measured S-parameters shown in Fig.4.

⁵ I. Iñiguez-de-la-Torre, J. Mateos, T. González, D. Pardo, J. S. Galloo, S. Bollaert, Y. Roelens, and A. Cappy, “Ballistic nano-devices for high frequency applications,” *Semicond. Sci. Technol.* 22, 663 (2007).

⁶ G. Deligeorgis, M. Dragoman, D. Neculoiu, D. Dragoman, G. Konstantinidis, A. Cismaru, and R. Plana, “Microwave propagation in graphene,” *Appl. Phys. Lett.*, vol. 95, no. 7, p.073107, 2009

Noteworthy is that the model as described so far, could not correctly predict the frequency dependence shown in the measured S-parameters. The low frequency experimental results show an abnormally high reflection coefficient. During fabrication, the signal and ground electrodes are deposited using a lift-off technique and PMMA e-beam resist. This is known⁷ to leave a thin residual layer less than 2nm in thickness. Such a PMMA layer is expected to act as a leaky capacitor connected in series with the Y-junctions thus hindering the low frequency coupling between the coplanar waveguide and the graphene at low frequency. To model this effect we have included a capacitor between the graphene layer and the CPW electrodes in the HFSS model. As shown in Fig.5, the correct frequency dependent behaviour is obtained.

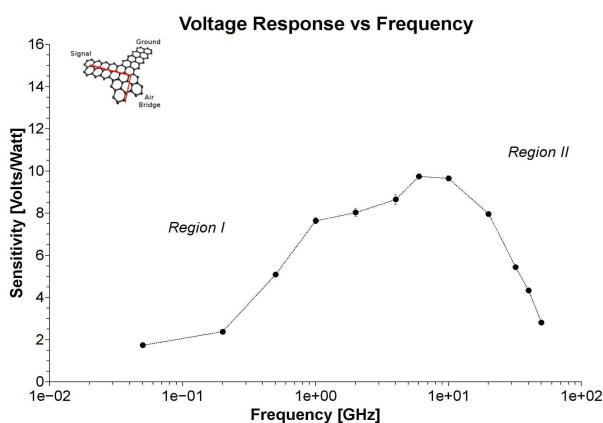


Figure 5: Room temperature DC response as a function of input frequency. The inset shows the Y-junction shape with a possible electron trajectory

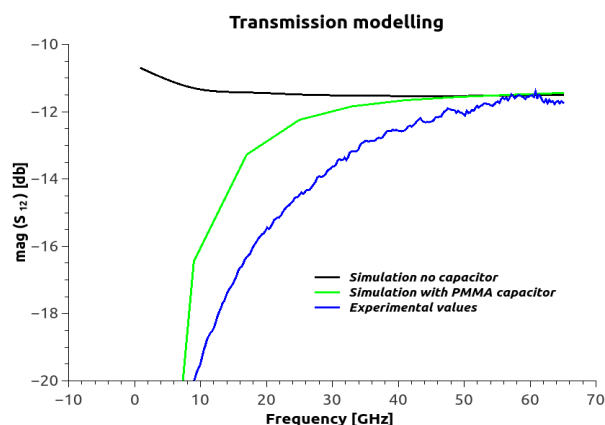


Figure 6: Transmission results. Without the PMMA capacitor the transmission is strongly deviating from the measured values.

Simulation of the device was done for a graphene sheet resistance value of 1900 Ohm/sq. Taking into account the fact that a large contact resistance exists between the metal electrodes and the graphene the actual sheet resistance of the graphene layer is in fact significantly smaller. Finally the PMMA capacitor taken into account is 1nm thick. To precisely model the effects identified by the HFSS simulation, we have used the equivalent circuit analysis shown in Fig.7. Initially the reference device was modeled ignoring the branches highlighted in amber boxes. Subsequently, the actual device was modeled adjusting only the graphene related components. The green highlighted branches relate to losses towards the substrate. R_{gg} is the graphene resistance, R_{gmi} is the metal-graphene ohmic contact resistance corresponding to the input electrode and R_{gmu} is the metal-graphene resistance that corresponds to the output electrode. Those resistances are different since the electrode geometry is not symmetric. Similarly C_{gm} is the capacitance due to the PMMA residual layer denoted in a similar manner. Finally C_T is the capacitance of the input output electrode coupling and R_s the resistance of the metallic parts.

Using the values shown in Fig.7 an excellent fit with measured values is achieved as shown in Fig.8. The calculated R_{gm} is in the vicinity of 1 KOhm which compares well to typical resistance values obtained in the literature. Furthermore, R_{gg} computed value is 225 Ohm which if we take into account the geometry of the device (Ground – signal distance and graphene coverage due to Y-junction patterning) leads to a graphene sheet resistance comparable to HFSS results.

⁷ Y.-C. Lin, C. Jin, J.-C. Lee, S.-F. Jen, K. Suenaga, and P.-W. Chiu, "Clean Transfer of Graphene for Isolation and Suspension," *ACS Nano*, vol. 5, no. 3, pp. 2362–2368, Mar. 2011.

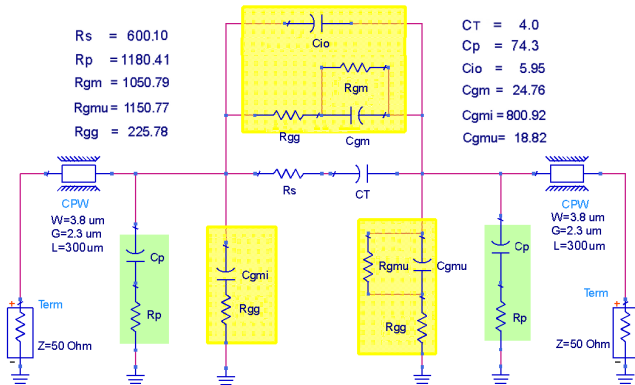


Figure 7: The Equivalent model used to simulate the RF behavior of the device. The components to correctly model the reference device are marked in green and the components added to model the graphene Y-junctions behavior are marked with amber. All resistances are in Ohm and Capacitance values in femtoFarad.

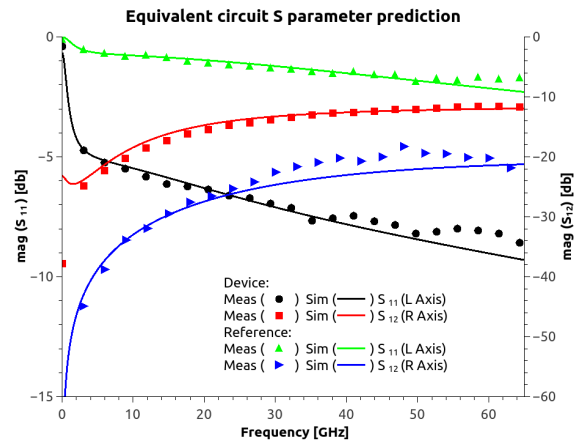


Figure 8: Comparison of S parameters predicted by the EC model (lines) with the measured values (datapoints) for the reference and the final device. The phase results (not shown here) are also in excellent agreement.

4.2 DEVICE OPTIMIZATION

Based on the results of the previous section, the first step to optimize the device performance is to remove the residues existing between the metallic electrodes and the graphene layers. This will reduce the contact resistance (R_{gm}) as well as reduce the “capacitor” effect dramatically affecting the low frequency coupling of the RF field into the graphene Y-junction nanoribbons.

To complete the optimization we have investigated the effect of the graphene sheet resistance. For the case where the total sheet resistance is reduced to 700 Ohm/sq, the device exhibits a $S_{11} < -14$ dB and an $S_{21} < -9$ dB. Conversely, keeping the sheet resistance intact, the number of Y-junctions would have to be increased to obtain better matching.

Finally, the electric field in the nanoribbon area was plotted and is shown in Fig.9.

As shown, the maximum electric field is actually in the vicinity of the foot of the bridge structure thus indicating that the distance between the adjacent Y-junctions should be increased. This is expected to improve the field distribution in the center of the junction and thus the performance of the device.

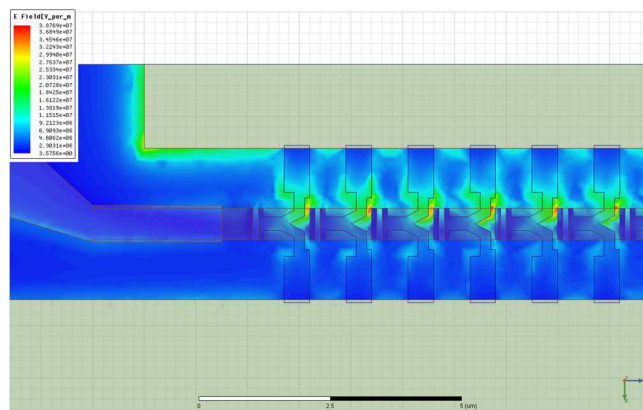


Figure 9: E field chromatic representation showing the highest field existing in the structure

5 DESIGN AND FABRICATION OF THE GRAPHENE COPLANAR PATCH ANTENNA (CPA)

The graphene coplanar patch antenna (CPA) is a new type of antenna based on a graphene monolayer. Its design was presented in the WP2. The rectangular resonator of the antenna is made of graphene, while the CPW structure is made of 400-nm thick gold. The graphene antenna was fabricated on the CVD-grown graphene wafer having a Si/SiO₂ substrate with a thickness of 500 μm/300 nm, respectively.

Figs. 10a-10b show the CST MWS design of the graphene CPA with the main dimensions, whereas Fig. 10c displays the optical image of one of the fabricated prototypes.

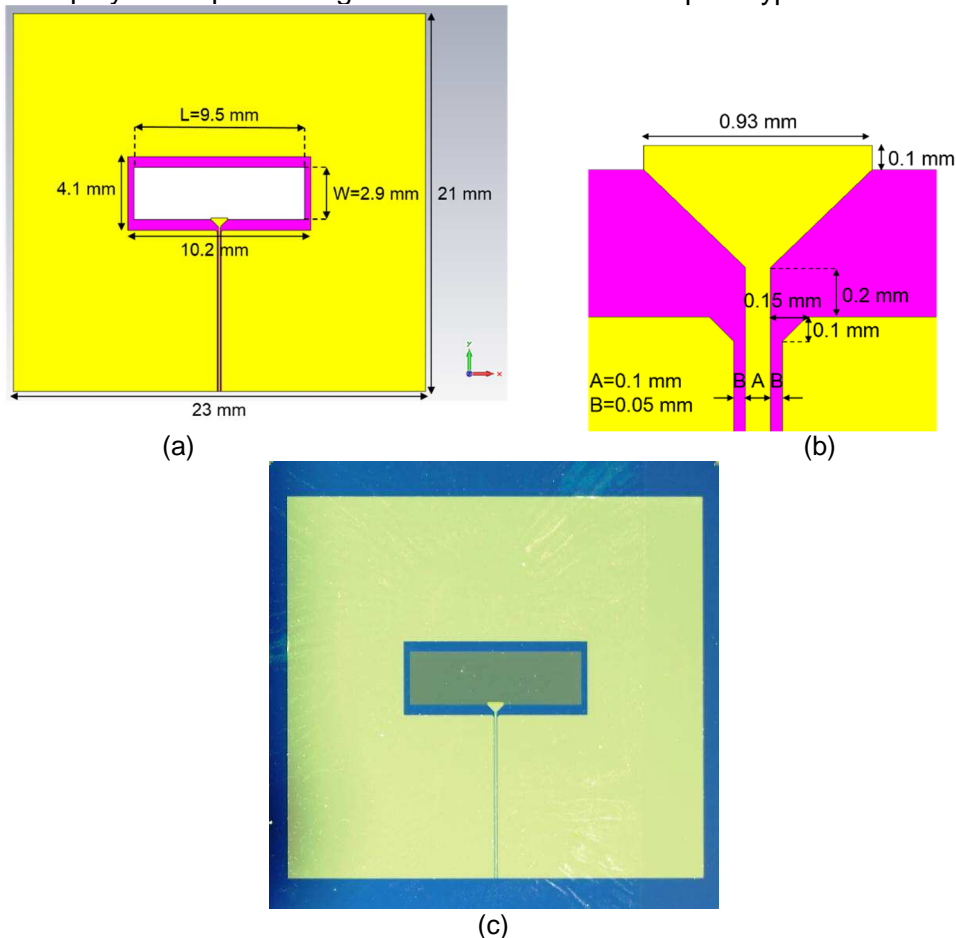


Fig. 10: (a) CST MWS design (with main dimensions) of the graphene CPA; (b) detail of the feeding point; (c) optical image of the fabricated graphene CPA.

The description of fabrication process of the graphene CPA was reported last year in the deliverable report D3.6 and will be not reproduced here again. In the following, we will provide the results of the RF measurements performed on the fabricated graphene CPA under various DC bias voltage values applied to the graphene resonator via a top electrode in a back-gate configuration. The graphene antenna was tested by considering its return loss and the radiation diagrams at different frequencies. Finally, an equivalent circuit model by means of AWR will be proposed to further characterize and validate the fabricated device.

6 EXPERIMENTAL CHARACTERIZATION OF THE GRAPHENE COPLANAR PATCH ANTENNA (CPA) AT MICROWAVE FREQUENCIES

We measured the reflection parameter $|S_{11}|$ as a function of frequency (f) using an on-wafer probe station linked to an Anritsu-37397D Vector Network Analyzer (VNA). The SOLT (Short, Open, Load and Thru) calibration was performed to calibrate the VNA before measurements. A CS-5 standard CPW calibration kit was used. The graphene-based antenna is DC biased using the probe station ground-signal-ground (G-S-G) probe tips. So, the DC voltage is applied between the central conductor and the grounds of the CPW using the internal bias tee of the VNA coupled to a Keithley 4200-SCS (Semiconductor Characterization System) able to provide controllable voltage/current sources. The antenna is fixed on a metallic plate playing the role of a backside metallization.

The results are displayed in Fig. 11 for the X band (8-12 GHz). We see an overall reflection loss of about -9 dB and two resonances located at 8.8 GHz and 11.4 GHz, corresponding to $|S_{11}|$ minimum values of -12.2 dB and -13.4 dB, respectively, at 0 V applied DC bias (solid black trace in Fig. 11). We see that the entire S_{11} dependence on frequency is shifted up and down depending on the applied voltages, while the resonances are shifted left or right with about 24 MHz. This is due to the fact that the surface resistance of the antenna is decreasing at 50 V and, respectively, increasing at -200 V. We see that, at 11.4 GHz, when the surface resistance is decreasing, the matching of antenna is improving with 1.5 dB while when the surface resistance is increasing we lose about 0.4 dB. The large values of the DC applied voltage are due to the fact that the slot widths are rather large: 350 μm on x-axis and 600 μm on y-axis (see Fig. 10a), and so the field applied between the graphene patch and the coplanar ground is rather small.

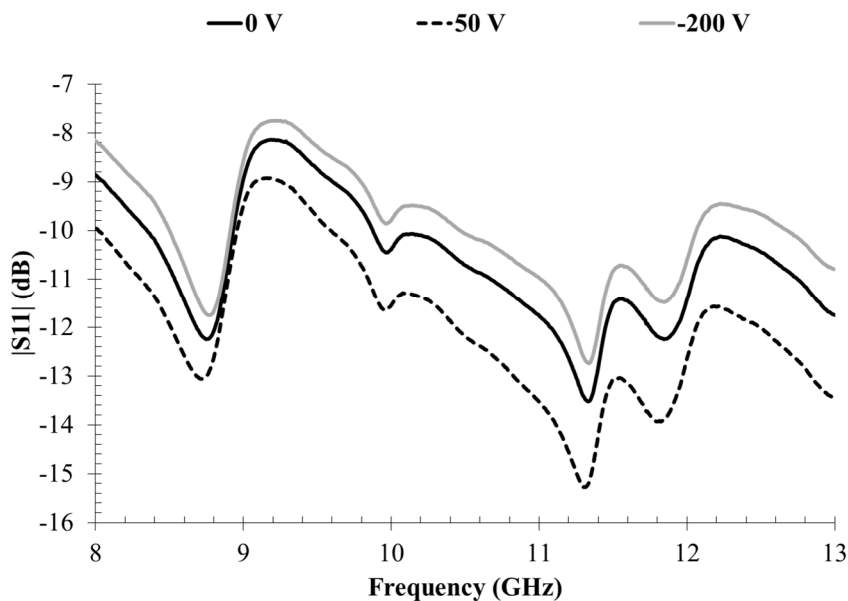


Fig. 11: $|S_{11}|(f)$ in the X band for three different bias voltages: 0 V (solid black trace), 50 V (dashed trace), and -200 V (solid grey trace).

The radiation pattern of the graphene antenna was measured using the setup from Fig. 12. The antenna was contacted on wafer with a G-S-G probe and used as emitter. It was fed by a PSG Analog Signal Generator (Agilent E8257C) with a 6-15 GHz microwave signal, modulated in amplitude (10 kHz square AM). A X-band waveguide flange was placed at a distance of 150 mm (satisfying far-field conditions in the X-band) and connected to a 10 MHz-40 GHz detector (Anritsu). The detected signal is amplified by a SR560 LNA and plotted on an oscilloscope (Tektronix DPO2024). Since the antenna has a thickness of 500 μm , much smaller than the microwave radiation

wavelengths, which are of the order of few cm at least, the antenna will not only radiate above the radiation plane represented by slots but also below, thus reducing the radiation efficiency. So, we have measured the detected signal at the position (0,0) – perpendicular to the metallization – in two conditions: (i) placing a microwave absorbent on the backside of the antenna and (ii) placing a metallic surface on the backside of the antenna. The 2D radiation patterns in the H-plane (orthogonal to the feed line of the antenna) were recorded at 7 GHz and 12 GHz in the case of the graphene-based antenna with a backside metallized surface (see Figs. 13 and 14), and at 8 GHz, 10 GHz, and 12 GHz in the case of the graphene-based antenna with a backside absorbent (see Fig. 15 for the X-band central frequency, i.e. 10 GHz). The 3 dB beamwidth (when the received power is reduced by half compared to the maximum) is between 40° and 80° for the radiation patterns presented in Figs. 13-15. In the case of the graphene-based antenna having a backside metallization, there are no side lobes at 7 GHz with one side lobe appearing at 12 GHz, meaning that part of the radiated microwave signal travels through the substrate towards the backside metallization and is then reflected back, being added with the frontside radiated signal. For the backside absorbent case, although the effects of the backside radiation are strongly diminished, multiple side lobes appear at 8 GHz and 12 GHz. The simulated gain of the antenna is -8 dB without backside metallization and -6 dB with backside metallization at 10 GHz. No calibrated gain measurements could be performed with the available equipment (see Fig. 12). The radiation efficiency and gain are weak but can be improved by reducing the sheet resistance of graphene. This can be achieved by optimizing the technological process and the antenna topology, including the graphene DC bias configuration. In our case, we have biased graphene with a DC electric field via coplanar configuration so the electric field is tangential to the graphene surface.

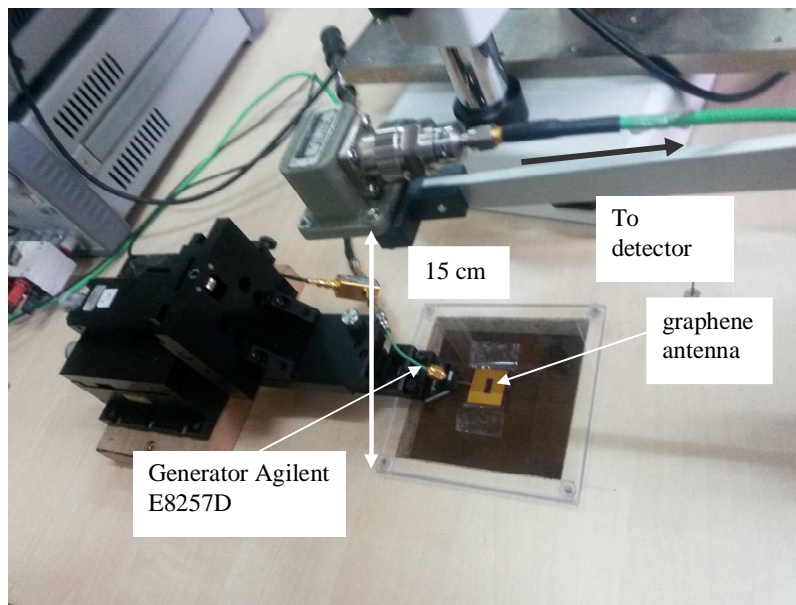


Fig. 12: radiation pattern measurement setup for the graphene CPA.

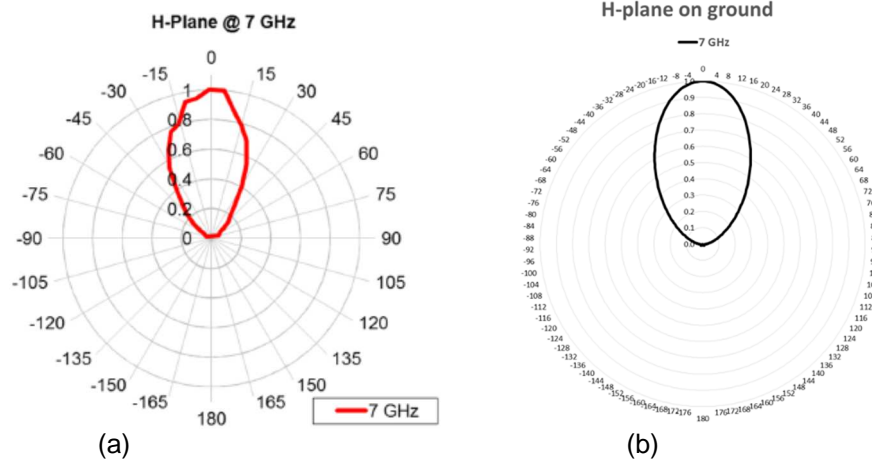


Fig. 13: radiation pattern of the graphene-based antenna with a backside metallization normalized at the maximum value at 7 GHz. The simulated 3 dB beamwidth is 69.4°.

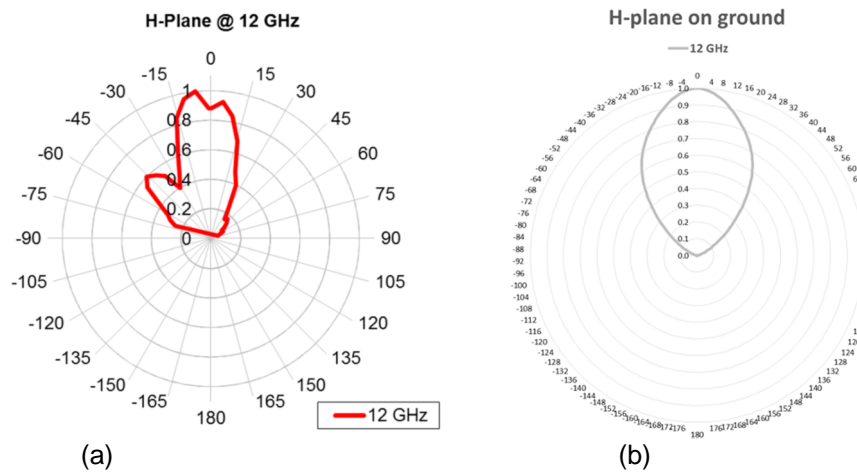


Fig. 14: radiation pattern of the graphene-based antenna with a backside metallization normalized at the maximum value at 12 GHz. The simulated 3 dB beamwidth is 76.5°.

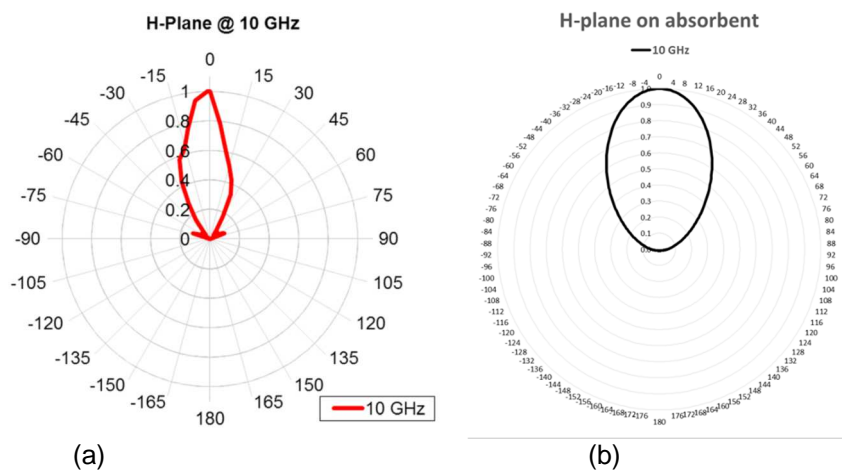


Fig. 15: radiation pattern of the graphene-based antenna with a backside microwave absorber normalized at the maximum value at 10 GHz. The simulated 3 dB beamwidth is 77.2°.

Finally, in order to understand the behavior of the graphene antenna, we used the equivalent circuit from Fig. 16, which was analyzed with AWR Microwave Office. The equivalent circuit is an R - L - C series circuit, where $R = R_s$ is graphene's surface resistance and $L = L_s = L_k$ is graphene's surface kinetic inductance. In the unbiased case, $L_k = 0.3$ nH, which corresponds to a reactance at 10 GHz equal to $X_s = \omega L_s = 19 \Omega$. Furthermore, R_s is 120Ω for the unbiased case, and $C = 1.104$ pF is the total calculated capacitance between graphene and the underlying metallic surface used for measurements. A CPW transmission line with the length of 9.55 mm and gap-signal-gap of 50-100-50 μm (with a characteristic impedance of 50Ω) is used to feed the antenna and inserted as a component in the equivalent circuit from Fig. 16. The metal thickness is 400 nm, and the thickness of the dielectric substrate is 500 μm . In Figs. 17a and 17b, we show the measured and simulated input impedance and the S11 (respectively), and we see that the experimental results fit quite well with the simulated ones. From these latter curves, we can extract more precisely the impedances corresponding to the resonances of S11 (they are represented on the Smith chart by closed loops towards the center of the diagram). We have the first resonance at 8.748 GHz ($|S_{11}| = -12.24$ dB), corresponding on Smith chart to $R = 31.56 \Omega$ and $X = -7.734 \Omega$, and the second resonance located at 11.34 GHz ($|S_{11}| = -13.51$ dB), corresponding on the Smith chart to $R = 67.57 \Omega$ and $X = 17.91 \Omega$. We see that the matching is not perfect but could be improved easily, since the reactive part is small, and the real parts are not far located from 50Ω . The matching can be further improved with a more complex matching network.

A further improvement of the proposed graphene antenna is currently on going and is based upon a thinner HR Si layer (down to 100 μm) under the graphene resonator. This way, it is possible to deposit a backside metal (gold) electrode – using backside lithography – in order to apply the DC bias perpendicularly, since this is the most effective way to change graphene's surface conductivity.

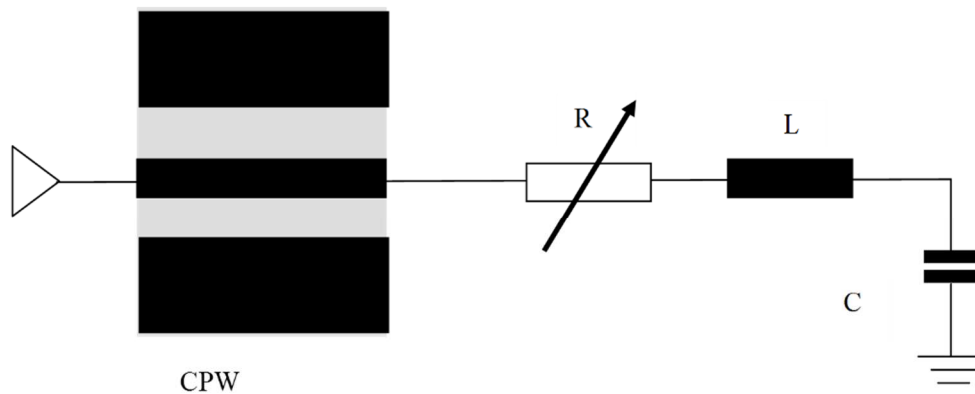
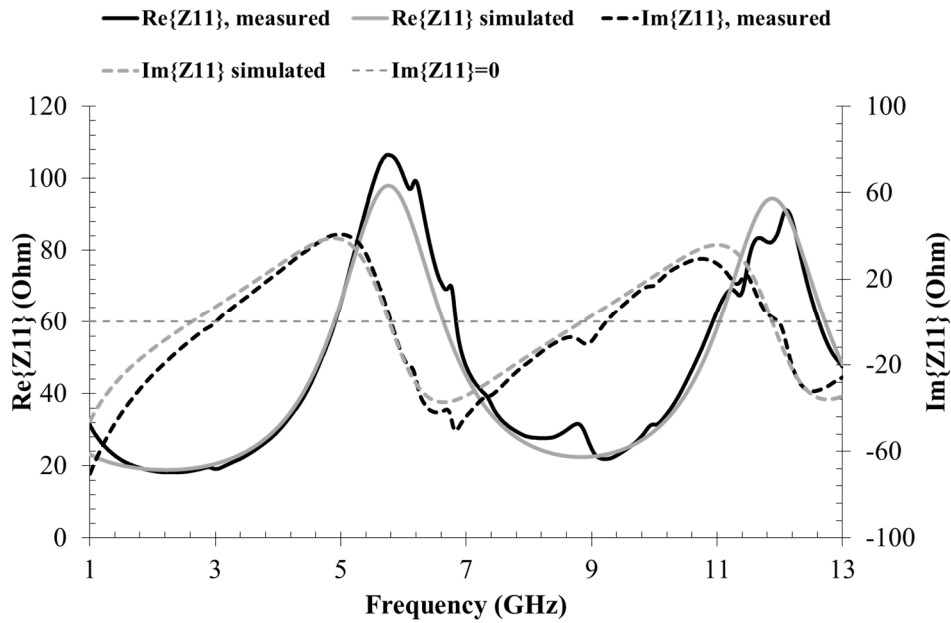
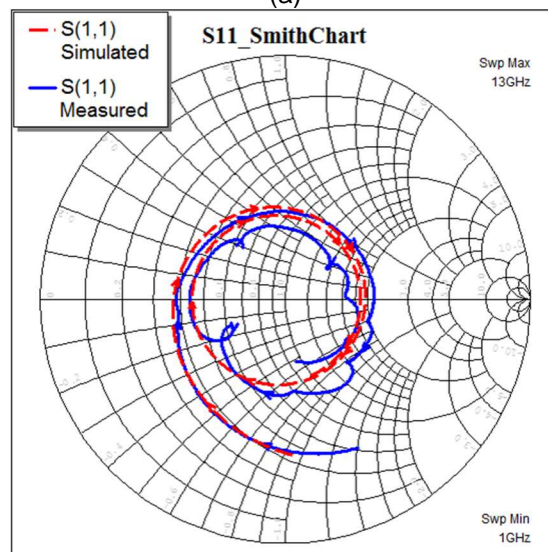


Fig. 16: AWR equivalent circuit of the graphene antenna.



(a)



(b)

Fig. 17: (a) Measured and AWR simulated input impedance of the antenna; (b) measured and AWR simulated S11 represented on the Smith Chart at 0 V.

7 THE X BAND SLOT ANTENNA LOADED WITH A GRAPHENE PATCH

7.1 ELECTROMAGNETIC MODEL AND SIMULATION RESULTS

Slot antennas, loaded with graphene patches, placed between the metallic strip and the surrounding ground plane, in different configurations, were described in D3.6. In the current reporting period the configuration with one graphene patch placed opposite the coplanar waveguide (CPW) feed line was optimized and test structures were fabricated and characterized. The results were presented at the European Microwave Conference in 2015 [1].

In this configuration, the bias is no longer applied using a back gate approach. Instead, the bias is applied directly through the CPW feed. By varying the conductivity of the graphene patch the electric field distribution inside the antenna slot can be controlled.

A fully parametric 3D electromagnetic model was developed using CST MWS (Fig. 18). A 0.2×0.2 mm² graphene patch is placed in the slot, between the metal strip and the surrounding ground plane, opposite the CPW feed line. The bias is applied at the same time as the RF signal, through the ground-signal-ground (G-S-G) probes of the Vector Network Analyzer (VNA), with the aid of a bias tee.

The graphene was modeled as a tabulated surface impedance, with the sheet resistance and reactance defined as parameters which could then be varied during the simulations. The substrate is high resistivity ($\rho = 5$ k Ω cm; $\epsilon_r = 11.9$) silicon of 525 μ m thickness and the chosen metallization is gold ($\sigma = 4.37 \cdot 10^7$ S/m). The structure is excited with a multipin rectangular waveguide port.

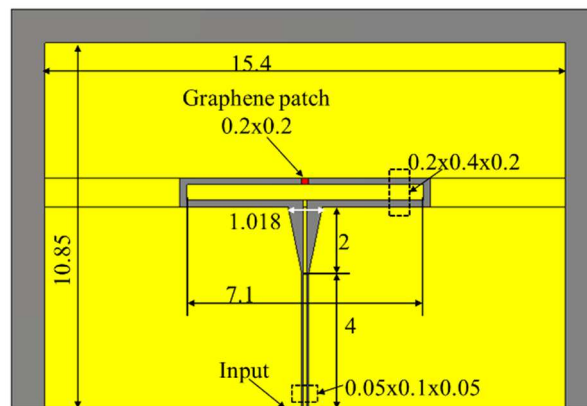


Fig. 18. Electromagnetic model and general layout dimensions of the X band slot antenna with a graphene patch (all dimensions are given in millimeters).

Fig. 19a shows the simulated S11 parameter as a function of frequency for various sheet resistance (R_{sq} parameter) values. The reactance (X_{sq}) was considered negligible, since the operating frequency is only 10 GHz [2]. Fig. 19b shows a detail of the resonance frequency, demonstrating the tuning effect of the graphene patch.

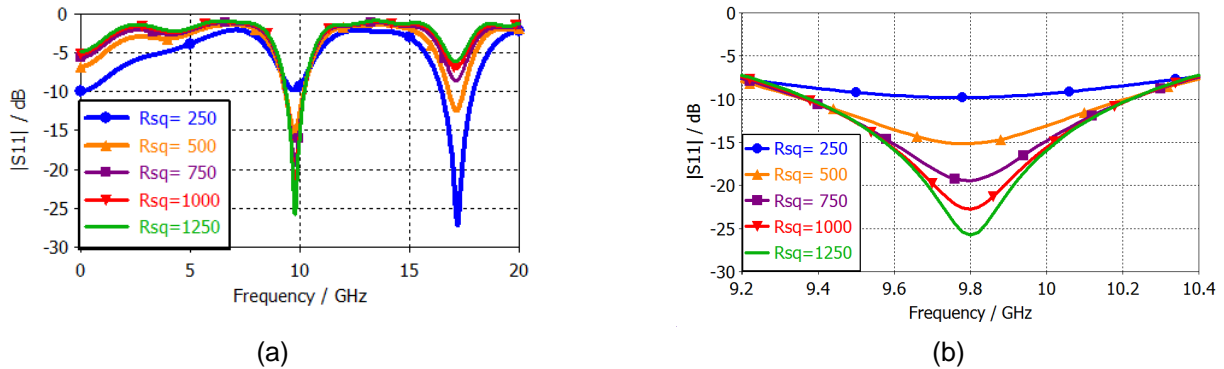


Fig. 19. Simulated S11 parameter for various sheet resistances (R_{sq}): (a) wideband frequency response; (b) detail of the tuning effect.

Other important antenna parameters are the radiation efficiency (Fig. 20a) and the antenna gain (Fig. 20b). Even though the efficiency deteriorates when $R_{sq} = 250 \Omega/\text{square}$ it is still better than 30% at 10 GHz. Fig. 20c shows the $|Z_{11}|$ parameter simulated for various sheet resistance values of the graphene patch.

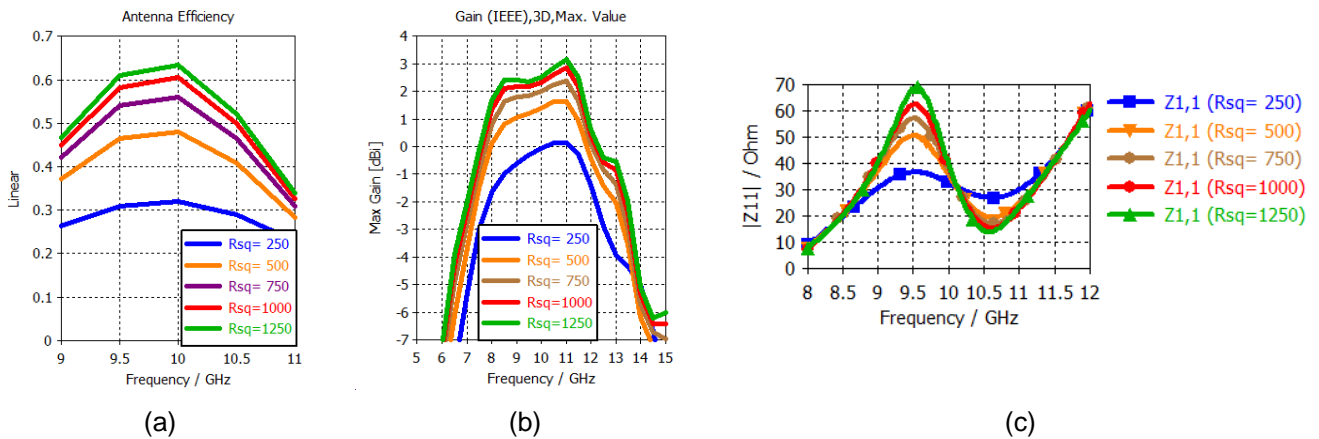


Fig. 20. Simulation results for different sheet resistance values of the graphene patch: (a) antenna efficiency – linear scale; (b) maximum gain; (c) $|Z_{11}|$ parameter.

Since the slot is the main radiating element and the graphene patch is only $0.2 \times 0.2 \text{ mm}^2$ the radiation is not severely impeded by it, with gains as high as 3 dBi for a high sheet resistance (1250 Ω/sq). This is also proven by the high antenna efficiency (>60% at 10 GHz for $R_{sq} = 1250 \Omega/\text{sq}$). The simulated 3dB gain bandwidth is between 7.6 – 12.2 GHz.

Fig. 21 shows the E-Plane (defined along the feed line) and the H plane (orthogonal to the E plane) for two values of the sheet resistance. Since the gain also takes into account the mismatch losses, the antenna is not only tuned with respect to the input matching, but also with respect to its radiation capability.

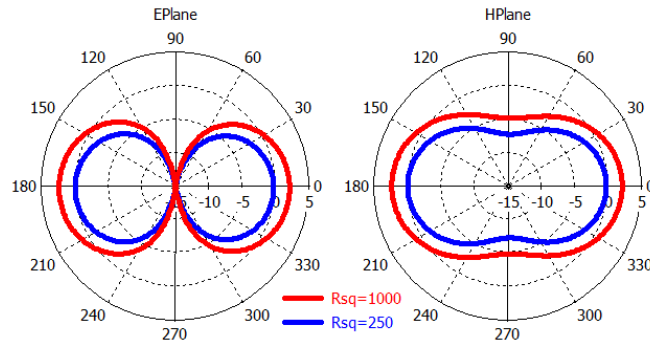


Fig. 21. E and H planes at 10 GHz for the sheet resistance (R_{sq}) of the graphene patch equal to 1000 Ω/sq (red trace) and 250 Ω/sq (blue trace).

There are two symmetrical main lobes, with no sidelobes. This is due to the fact that the high resistivity silicon substrate has a thickness of only 525 μm , much smaller than the wavelength in the dielectric (~ 8.7 mm).

7.2 MEASUREMENT RESULTS

Test structures were fabricated on a 525 μm thick high resistivity ($\rho = 5$ k Ωcm) silicon wafer. A silicon oxide layer of ~ 0.3 μm was grown through thermal oxidation, and graphene was fabricated by Graphenea (<http://www.graphenea.com/>) through chemical vapor deposition (CVD) and transferred over the whole Silicon wafer. Next, the graphene is patterned through reactive ion etching, followed by metal deposition and patterning. A thin (50 nm) Palladium layer is deposited first as adhesion layer, followed by a 0.3 μm Gold layer. A photo of the fabricated structure is shown in Fig. 22, with a detail of the graphene patch. The graphene patch was contacted through a metal-graphene overlap 0.2 x 0.02 mm² in size.

The antenna structure was characterized on-wafer using a Anritsu 37397D VNA with a PM5 Suss Microtec on wafer probing station. A standard on wafer short-open-load-thru calibration (1601 measurement points, four measurements averaged per point) was performed for the following frequency ranges: 0.04 – 20 GHz and 9 – 11 GHz.

The antenna was placed on absorbent material in order to reduce the effects of the back-side lobe. The bias voltage was applied using the internal bias tee of the VNA and a Keithley 4200-SCS (Semiconductor Characterization System). From DC current-voltage measurements the following differential resistances were measured: 700 Ω/sq at 0 V; 757 Ω/sq at -10 V and 833 Ω/sq at -20 V.

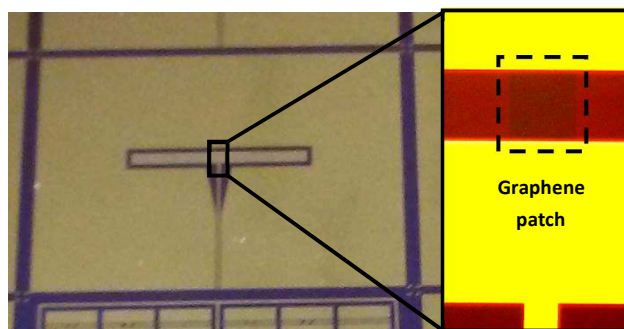


Fig. 22. Photo of the fabricated structure and a detail of the graphene patch.

Fig. 23 shows the measurement results for the three bias voltages, with a detail of the resonance frequency. The tunability effect is demonstrated by the experiments, with a 20 dB difference in amplitude of S_{11} and a 7.5 MHz frequency shift, as detailed in Table I.

Table I. Resonance Frequencies as a Function of Applied Voltage

Resonance frequency [GHz]	S11 [dB]	Applied voltage
9.85 GHz	-42.78 dB	0 V
9.845 GHz	-62.3 dB	-10 V
9.8425 GHz	-46.05 dB	-20 V

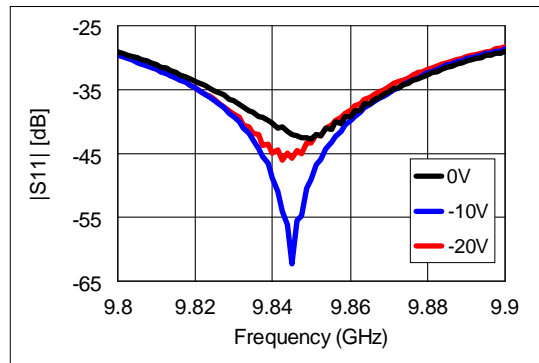
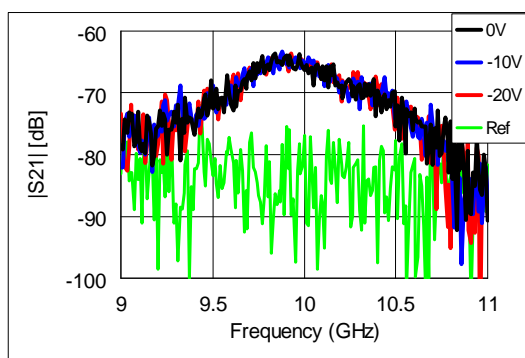
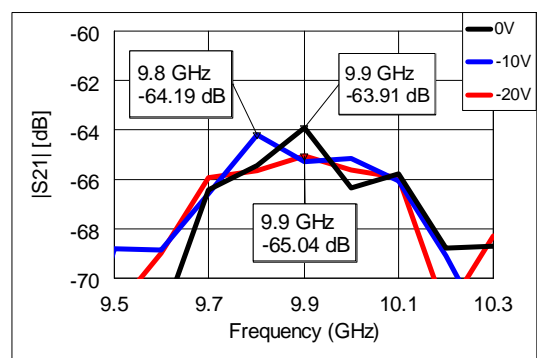


Fig. 23. Measured |S11| parameter for different biasing voltages.

In order to estimate the radiating properties of the antenna, a transmission measurement was also performed. The second probe of the VNA was suspended over the center of the antenna and the transmission was recorded. The reference trace is the recorded noise level of the VNA, for the two probes in the same position, but without contact to the antenna. The results are shown in Fig. 24a. Since the difference in sheet resistance is quite low (from 700 Ω /sq to 833 Ω /sq) and the value still large, the transmission is only slightly affected by the bias voltage. Fig. 24b shows a detail of the transmission characteristic, showing a difference of ~ 1 dB between the 0 V and -20 V bias (in good agreement with the simulations from Fig. 20b). Lower sheet resistances would lead to suppression of the radiation of the antenna in the X band. This could lead to a control of the maximum transmission range.



(a)



(b)

Fig. 24. Measurement transmission characteristic for different biasing voltages: (a) compared to reference transmission; (b) detail of transmission characteristic at different bias voltages.

References

- [1] A-C. Bunea, D. Neculoiu, M. Dragoman, G. Konstantinidis, G. Deligeorgis, "X Band Tunable Slot Antenna With Graphene Patch," Proceedings of the 45th European Microwave Week, EuMW2015, Paris, France, 6 – 11 September 2015, pp. 614-617.



D4.7: Activity Report on parameter extraction procedure for DC and HF models for CNT based sub-modules

20/21

[2] Perruisseau-Carrier, J.; Tamagnone, M.; Gomez-Diaz, J.S.; Carrasco, E., "Graphene antennas: Can integration and reconfigurability compensate for the loss?," Proceedings of the 43th European Microwave Week, EuMW2013, Nuernberg, Germany, 6 – 10 October 2013, pp. 369-372.

8 CONCLUSION & PERSPECTIVES

For the Graphene demodulator an electromagnetic model has been developed and used to simulate and model the graphene based ballistic demodulator designed and fabrication within the NANORF project. Based on these results, device performance has been explained and several optimization points have been clearly identified. The presented work is the first to simulate such a device and propose ways to improve performance.

... other device conclusion required from UNIVPM, UPMC, IMT and FORTH